Grey Angus (Orcid ID: 0000-0002-1540-1080)

Detection of small molecule concentration gradients in ocular tissues and humours

Berin A. Boughton[1], Oliver R.B. Thomas[2], Nicholas J. Demarais[3], Dennis Trede[4], Stephen E. Swearer[2], Angus C. Grey[5]

[1]Metabolomics Australia, [2]School of BioSciences, University of Melbourne, Melbourne, Australia, [3]School of Biological Sciences, University of Auckland, Auckland, New Zealand, [4]Bruker Daltonik GmbH, Bremen, Germany and [5]School of Medical Sciences, University of Auckland, Auckland, New Zealand

Corresponding Author:

Angus C Grey, PhD
School of Medical Sciences
University of Auckland
Email: ac.grey@auckland.ac.nz
Ph: +64 9 923 3174

Abbreviations:

MALDI – matrix-assisted laser desorption/ionisation; IMS – imaging mass spectrometry; FT-ICR – Fourier Transform Ion Cyclotron Resonance; MS/MS – tandem mass spectrometry; AH – aqueous humour; VH – vitreous humour; GSH - glutathione

Key words:

MALDI imaging mass spectrometry, eye, lens, retina, metabolites, humours

ABSTRACT

The eye is an elegant organ consisting of a number of tissues and fluids with specialised functions that together allow it to effectively transmit and transduce light input to the brain for visual perception. One key determinant of this integrated function is the spatial relationship of ocular tissues. Biomolecular distributions within the main ocular tissues cornea, lens and retina have been studied extensively in isolation, yet the potential for metabolic communication between ocular tissues via the ocular humours has been difficult to visualise. To address this limitation, the current study presents a method to map spatial distributions of metabolites and small molecules in whole eyes, including ocular humours. Using a tape-transfer system and freeze-drying, the spatial distribution of ocular small molecules was investigated in mouse, rat, fish (black bream) and rabbit eyes using negative ion mode MALDI imaging mass spectrometry. Full-scan imaging was used for discovery experiments, while MS/MS imaging for identification and localisation was also demonstrated. In all eyes, metabolites such as glutathione and phospholipids were localised in the main ocular tissues. In addition, in rodent eyes, major metabolites were distributed relatively uniformly in ocular humours. In contrast, both uniform and spatially-defined ocular metabolite distributions were observed in the black bream eye. Tissue and ocular humour distributions were reproducible, as demonstrated by the three dimensional analysis of a mouse eye, and able to be captured with high spatial resolution analysis. The presented method could be used to further investigate the role of inter-tissue metabolism in ocular health, and to support the development of therapeutics to treat major ocular diseases.

INTRODUCTION

Imaging mass spectrometry (IMS) using matrix-assisted laser desorption/ionisation (MALDI) is now an established imaging modality for the spatial mapping and relative quantitation of proteins, peptides, lipids, pharmaceuticals, metabolites and some post-translational modifications [1-7]. Originally demonstrated by detecting peptide distributions in the rat pancreas and pituitary gland [1], MALDI-IMS has been applied to a wide range of biological tissues from many organisms. In a typical MALDI-IMS experiment, tens to hundreds of individual analytes are detected and spatially mapped simultaneously from a single thin tissue section, allowing their relative abundance across the section, and their spatial relationship to other analytes within the tissue section to be measured. While this has been useful in some tissues for protein and peptide analysis, with subsequent verification using antibody labelling and optical microscopy detection methods[8], the application of MALDI-IMS to study analytes for which no specific antibodies exist, such as lipids and metabolites, is particularly exciting.

One challenge in tissue preparation for MALDI-IMS is the routine generation of high-quality tissue sections, particularly from tissue that is highly biochemically heterogeneous or contains air- or fluid-filled compartments. Generally, MALDI-IMS is performed on fresh frozen tissue sections, and embedding media used routinely in sectioning for e.g. optical microscopy, such as optimal cutting temperature compound (OCT), is not recommended primarily due to its PEG composition and the subsequent ionisation and detection of this compound in the low mass range by MALDI mass spectrometry[9]. While many fresh frozen tissues lend themselves to cryosectioning, such as the brain presumably due to its high fat content, other tissues are not as conducive to cryosectioning, such as the ocular lens which contains tissue regions with very different hydration and mechanical

properties. The challenge is even greater when the experiment requires the generation and analysis of whole bodies or whole organs, such as the eye, which contain tissues of multiple different densities, hydration states, and biochemical composition. A number of strategies have been demonstrated to improve the sectioning of delicate tissue for subsequent MALDI-IMS analysis. Embedding using alternative compounds to OCT, such as ice[10], gelatin[11], and carboxymethylcellulose[12], support the exterior of the cryosection, but do not support intricate structures within the tissue. Tissue fixation by chemical cross-linking agents, such as paraformaldehyde, have also been demonstrated. While this has a limited effect on ionisation of some molecules, such as N-glycans[13, 14] and some phospholipid classes[15], the detection of proteins can be perturbed and require additional tissue preparation steps, such as on-tissue enzymatic digestion[16, 17] to restore protein detection via peptide mapping. The effect of either chemical or dehydration fixation of tissues on metabolites is less clear, although one study showed that ~72% of metabolite distributions are retained after the fixation process.[18]

The moment of section collection is also crucial for generation of cryosections that will produce high quality MALDI-IMS data. For collection of delicate tissue, such as the ocular lens, both a methanol landing strategy, where a thin film of methanol is applied to the MALDI target plate just prior to section collection[19], and double-sided, electrically conductive carbon tape to physically stick the section to the tape[20] have been successful. In the case of methanol landing, the concern is that small molecules may be delocalised during the section collection process if the methanol volume is excessive. Finally, stabilisation of the tissue section prior to cutting, by using a tape transfer system[10, 21] has been useful for the collection of fresh frozen sections from some tissue types. Recently, methods for collection and MALDI-IMS analysis of plant tissue sections using tape transfer[22, 23] were reported. Importantly, while the transfer tape is non-conductive, analysis of small molecules and

metabolites was possible using MALDI-FT-ICR mass spectrometry, for which the use of a conductive target plate is not required.

The eye is a highly specialised, delicate organ that contains a variety of tissues and fluids that facilitate vision. Major structures include the main, transparent light focussing elements (cornea and lens), the photoreceptor cells which transduce light into electrical signals (retina), and the ocular fluids (humours). The vitreous humour (VH) provides structural properties to the ocular globe and interfaces posteriorly with the retina, and anteriorly with the posterior surface of the lens. The aqueous humour (AH) bathes the anterior surface of the lens and nourishes the specialised tissues of the anterior eye to maintain intraocular pressure homeostasis and the refractive and optical properties of the eye. The metabolic constituents of these important ocular fluids have been studied previously in healthy eyes and in disease models by both NMR[24, 25] and MS-based[26, 27] approaches. However, these studies have not maintained any spatial information. Previously, specific tissues of the eye have been dissected, isolated, and subjected to MALDI-IMS analysis. Proteins[19, 28-31], peptides[32], lipids[33-35], and metabolites[36-38] have been studied in the ocular lens of a range of species to understand the effects of aging on the lens and implications for lens cataract formation. In the retina, both layer analysis via lipid detection[39, 40], and surface analysis of retinal flat mounts using metabolite detection[41-43] have been studied to investigate some of the mechanisms involved in macular degeneration[44]. Analysis of the whole eye has also been demonstrated for lipids[45], oligonucleotides[46], and used to trace drug penetration and movement in the eye[47-50]. However, a limitation of these whole eye studies is the lack of spatial information in the ocular humours themselves. This information could have particular interest to both functional studies of how the eye acts as an integrated organ, and in the analysis of drug administration and penetration. In this study, we aimed to develop a method to allow MALDI-IMS analysis of whole, unfixed eyes that maintained

the spatial relationships of all major ocular tissue structures and the aqueous and vitreous humours, and that could be applied to eyes from a range of species using a variety of metabolite MALDI matrices.

MATERIALS AND METHODS

Tissue and Reagents

All reagents were purchased from Sigma-Aldrich (St Louis, MO). Juvenile black bream (*Acanthopagrus butcheri*) were caught *via* otter trawl in the Gippsland Lakes, Australia (37°51'28.3572''S, 147°44'39.0984''E) in July 2017. Adult bream were caught *via* gill net on the Werribee River, Australia (37°57'45.6"S, 144°40'02.9"E) in March 2018. Fish were measured (juveniles, 5-7 cm fork length; adults 30-38 cm fork length), euthanised and decapitated at the first cervical vertebra. Following decapitation, the eyeballs were carefully incised from the skull and individually stored on dry ice in labelled falcon tubes. Upon return from the field, all samples were stored at -80 °C at the University of Melbourne. Fish were collected under Arthur Rylah Institute Animal Ethics Committee approval 14/12 and the State of Victoria, Australia Department of Environment and Primary Industries' Fisheries research permits #1135 and #1204. Wild-type mouse eyes (C57Bl/6, 23 weeks) were obtained from the carcass of a mouse that had been culled as part of an experiment conducted with approval from the Animal Ethics Committee of the Florey Institute of Neuroscience and Mental Health (FINMH-17-055). Eyes from Wistar rats (p21) were obtained from animals that had been culled by CO_2 asphyxiation and decapitation as part of an experiment conducted with approval from the University of Auckland Faculty of Medical and Health Sciences Animal Ethics Committee (AEC 001748). Eyes from New Zealand white rabbits (*Oryctolagus cuniculus,* weight 5.5kg) were obtained from the carcass of a rabbit that had been culled by anaesthesia (i.v. pentobarbital overdose) as part of an experiment conducted with approval from the University of Auckland Faculty of Medical and Health Sciences Animal Ethics Committee. Whole eyes were removed immediately following death, and frozen using one of several gentle freezing

strategies to avoid sample cracking. Techniques used were liquid nitrogen vapour freezing, placing tissue in a -80 °C freezer, or dipping the embedding tool holding the sample into an isopropanol dry-ice slurry. Where required, samples were stored on dry ice before being transferred to a -80 °C freezer for storage until use.

Tissue sectioning and preparation

Sectioning supplies including Menzel-Gläser Superfrost Ultra Plus Glass slides, Optimal Cutting Temperature (OCT) compound and Feather® C35 tungsten microtome blades were purchased from Grale HDS (Ringwood, Australia). Fresh-frozen eyes were embedded in carboxymethylcellulose (CMC, 2%) and mounted on cold specimen holders using CMC. Eyes were oriented lateromedially in order for collected cryo-sections (20-50 μm thick) to contain the entire light path. Once a smooth cutting plane was established, cryofilm (2C(9), Section-Lab Ltd, Japan) was applied to the cut surface, and a cryo-section cut. For the mouse eye 3D model every second 35 μm thick section was taken and applied to cryofilm. The cryofilm containing the cryo-section was attached to a pre-cooled glass slide with double-sided copper foil tape. Once multiple sections were collected on each glass slide, mounted tissue sections were transferred to a freeze dryer (Christ Alpha 1-4 LD plus Freeze Drier (John Morris Scientific, Australia) for 10–15 mins to remove water. Freeze-dried sections were then brought to atmospheric pressure and temperature then transferred to a vacuum desiccator for storage until matrix deposition.

Matrix Deposition

N-(1-naphthyl) ethylenediamine dihydrochloride (NEDC, 7mg/mL in 90% MeOH) or 1,8-bis(pyrolidinyl)naphthalene (BPYN, 5mg/mL in 100% acetone) was applied to the tissue sections

using a TM-Sprayer (HTX Technologies, Carrboro, NC). The spray settings for NEDC application were: solvent flow rate 0.1 mL/min, nozzle speed 1300 mm/min, nozzle temperature 30°C, track spacing 2mm, dry time 0.5 min, 4 passes with 90° rotation on passes 2 and 4. The spray settings for BPYN application were: solvent flow rate 0.15 mL/min, nozzle speed 1300 mm/min, nozzle temperature 30°C, track spacing 2mm, 1 mm offset for repeat passes, 8 passes with 90° rotation on passes 2, 4, 6 and 8. NEDC was used for rat, rabbit and black bream samples. BPYN was used for mouse samples. Following matrix deposition, samples were stored in a vacuum desiccator until data collection.

MALDI Imaging mass spectrometry

MALDI-IMS was carried out on a Bruker Solarix-XR 7T FT-ICR mass spectrometer (Bruker Daltonics, Billerica, MA) using flexImaging v4.1. MALDI-IMS data sets were collected in negative ion mode from *m/z* 50 – 1000, with a spatial resolution of 30-50 μm. Laser beam size was set to minimum, and a random movement within a 25–45 μm radius of each sampling location used to collect each mass spectrum, which was the sum of 300 laser shots. Black bream and mouse sample analysis at the University of Melbourne used a transient length of 2M across the mass ranges 100-2000, providing a mass resolving power of 130000 at m/z 400. Rat and rabbit sample analysis at the University of Auckland used a transient length of 1M across the mass ranges 100-1000, providing a mass resolving power of 66000 at m/z 400. Single eyeball section imaging times varied depending on sample size and spatial resolution, from ~30 min (mouse/rat) to ~150 min (rabbit). An additional mouse eye high-spatial resolution MALDI-IMS data set was collected on a Bruker MALDI timsTOF Flex (Bruker Daltonik, Bremen, Germany) operated in MS (QTOF) negative ion mode from *m/z* 200 – 2000, with a minimum laser spot providing a spatial resolution of 10 μm. Putative identification of signals detected in the MALDI-IMS datasets was made using database interpretation (LipidMaps, Metlin)

and online metabolite annotation via Metaspace (metaspace2020.eu)[51] of accurate masses matching to the HMDB, ChEBI, LipidsMaps and SwissLipids databases (Table 1). Tandem mass spectrometry experiments (CID) using the Bruker Solarix-XR mass spectrometer where possible were used to identify a subset of the observed metabolites, the spatial resolution was set to 100 µm with a random movement within a 95 µm radius, an isolation window of 10 *m/z* and CID energy of 25 V were used.

Data analysis

Data sets were imported into SCiLS Lab Pro (version 2019c, SCiLS GmbH, Bremen, Germany), each spectrum was normalised using the root mean square method, and MALDI images plotted at the predicted *m/z* +/- 0.005 Da with weak de-noising on for FT-ICR data and no denoising for timsTOF data. Three-dimensional data was assembled from registration of 2D data from serial sections. 3D registration was performed by manual shift and rotation transformation (so-called rigid image registration) based on ion images at *m/z* 885.5519. After ion images of *m/z* 885.5519 from all serial sections were registered, the whole cube of MALDI-IMS data was aligned using the same rigid transformation. Principal components analysis was computed on a subset of 37 annotated metabolites, error is represented at the 95% quantile. The selected 37 metabolites for PCA analysis were manually selected from metaspace annotation results of mid-eye sections (sections 18 and 19) representing a range of tissue localisations with signals from low-to-high mass range (see Table S1 *Supplemental Information*). For assignment of lipid identifications, precursor ion masses were loaded in to the LipidMAPS MS analysis tool to generate a list of possible identifications based on accurate mass. The LipidMAPS MS/MS spectrum prediction tool was then used to generate predicted MS/MS

spectra for each putative identification and each combination of fatty acid tail groups, and then manually matched with detected MS/MS spectra from imaged retinal regions.

RESULTS

The reproducible collection of thin tissue sections is crucial for generation of high quality MALDI-IMS data. This is particularly challenging for tissue that is highly biochemically heterogeneous or that contains air- or fluid-filled compartments. The aim of this study was to develop a tissue preparation method that allowed the reproducible collection of tissue sections from the whole eye, and to then map the spatial distributions of small molecules in the ocular tissues and humours using MALDI-IMS. We hypothesised that since the eye is an integrated organ, its humours would contain gradients of small molecules that may reflect local or inter-tissue communication between the major ocular tissues.

Initial experiments aimed at optimising eyeball sectioning utilised rat tissue. A variety of section thicknesses (20-70 μm) were trialled, however sections from whole fresh-frozen eyeball sections could not be collected consistently without additional sectioning aid. While the ability to study small molecule distributions from fixed tissue has been shown, generally these distributions have been generated from tissue areas[18, 52, 53]. Therefore, whole eyeball fixation (cross-linking or dehydration) was not considered since the more water-soluble small molecules and metabolites were unlikely to maintain their *in vivo* localisation during the fixation process, particularly in the highly aqueous ocular humours. A tape-transfer system (Cryofilm, Section-Lab, Japan) provided sufficient support for eyeball sections (20–50 μm thick, typically 35 μm was used) to be consistently collected and mounted on double-sided copper tape (Figure 1). Appropriate tissue section drying was then trialled (Figure 2) and sections coated with NEDC matrix. NEDC has previously been shown to work exceptionally well for the quantification of glutathione (GSH) and other small metabolites in lens tissues[36]. Application of NEDC also adds a 1:1 molar ratio of Cl anion allowing observation of a

significant number of Cl adducts. MALDI images of different classes of small molecules (putative sugar, peptide, nucleotide, lipid) were compared between rat eye sections dried at room temperature (Figure 2A-E) or freeze-dried (Figure 2F-J). Generally, within the spatial resolution parameters that the tissues were sampled at, small molecule localisation was maintained in freeze-dried sections, and delocalised following room temperature drying. The degree of delocalisation varied with tissue location and solubility of the analytes in water, the main solvent in biological tissue and ocular humours in particular. For example, putative glucose and GSH (identified by on-tissue MS/MS, see *Supplemental Information*) in the VH and lens, respectively (Figure 2B and 2C), are very water soluble (1200 mg/mL and 292.5 mg/mL, respectively) and were badly delocalised in room temperature-dried sections (Figure 2G and H). Interestingly, the intensity and localisation of putative glucose signal from the cornea (e.g. Figure 2B) was very similar between drying methods, although the cornea is difficult to distinguish from AH in the freeze-dried section since the signal intensity from AH and cornea is similar (Figure 2G). Putative adenosine mononucleotide (AMP), which localised to multiple ocular tissues but was enriched in the iris (Figure 2D), is less water soluble (10 mg/mL) and was less affected by room-temperature drying (Figure 2I). The spatial distribution of a putative phospholipid detected in the retina, which is not water soluble, was largely unaffected by the drying methodology (Figure 2E and J).

To test the suitability of the tissue preparation technique in different species, the eye from juvenile black bream (*A. butcheri*), a teleost fish, was used (Figure 3). There are some important differences between the mammalian eye and the teleost eye. For example, in the mammalian eye the lens is held in place by suspensory ligaments, while in the teleost eye the lens is suspended by a ligament on its superior surface and a muscle on its inferior surface. In the presented example, the ligament of the teleost eye is clearly identifiable above the spherical lens in the tissue section (Figure 3A,

asterisk). The common major anatomical regions (tissues and fluids) of the juvenile black bream eye were user defined in the analysis software (SCiLS Lab 2019c Pro, Bruker, Bremen), and the included co-localisation analysis pipeline used to highlight detected *m/z* ratios that were present in each region. While some abundant molecules were common between rat and black bream, a different set of black bream small molecule distributions are presented (Figure 3) that define similar ocular anatomical regions in the rat eye (Figure 2).

Many signals localised to major anatomical structures of the black bream. In the posterior eye, a signal at *m/z* 261.9428 was localised to the uvea (i.e. choroid and iris, Figure 3B) while a putative phospholipid detected at *m/z* 834.5264, phosphatidyl serine PS(40:6), was abundant in the neural retina (Figure 3C). The lens contained many signals localised to either the cortex, such as *m/z* 438.1429 (Figure 3D), or the nucleus, for example *m/z* 902.4642 (Figure 3E). Some signals were found in multiple tissues, such as *m/z* 196.0740, which was confirmed by on-tissue MS/MS as N-acetyl histidine (see *Supplemental Information*), a common small molecule found in fish tissue (Figure 3F). N-acetyl histidine was detected in the lens cortex and at lower levels in the neural retina and humours. A signal detected at *m/z* 426.0256, putative ADP, was localised to the lens, retina, and ocular musculature (Figure 3G). Interestingly, co-localisation analysis of the aqueous and vitreous humours gave a variety of different small molecule distributions within each ocular fluid. No *m/z* signal was found exclusively in the AH, however some *m/z* signals were more abundant in this fluid, (Figure 3I, *m/z* 374.9788). This *m/z* signal was not due to background signal from the cryofilm transfer tape, since cryofilm-associated *m/z* signals produced MALDI images that showed signal throughout both humours that was most intense in regions that contained no humour, i.e. where signal from cryofilm alone was being sampled (Figure 3H, *m/z* 405.1888, putative [octaethylene glycol+Cl]$^-$, a possible PEG component of the cryofilm). One *m/z* signal was closely associated with

the lens periphery (Figure 3J, *m/z* 380.0046), while several *m/z* signals showed distributions that were relatively uniform in the VH (*m/z* 385.0870, Figure 3L), or that were more abundant in the posterior region that interfaces with the retina (Figure 3K, *m/z* 411.9880). Any perceived dorso-ventral intensity differences (see Figure 3L) could be environmental, due to the majority of light entering the fish eye from above. Interestingly, several *m/z* signals were most abundant in the humour surrounding the iris. One distribution was relatively diffuse, with signal most abundant in the spaces between the iris and lens (Figure 3M, *m/z* 360.9983). A second distribution was more concentrated around both the anterior and posterior surfaces of the iris, which diminished but remained present in the VH (Figure 3N, *m/z* 504.0359). Together, these distributions suggest a complex mixture of small molecule gradients exist in the ocular humours of the teleost eye.

Having established whole eyeball MALDI imaging in small eyeballs, larger eyeballs from rabbits were tested for their compatibility with the protocol. The larger eyeball size allowed for overview MALDI imaging datasets to be collected at lower spatial resolution (200 μm), and more detailed investigation of specific regions of the eyeball (50 μm spatial resolution) due to their larger size (Figure 4). At the overview level, similar distributions were seen for the putative phospholipid PS(40:6) detected at *m/z* 834.5365 (Figure 4B) to the smaller eyeballs, where it was most abundant in the retinal tissue. The same was true for ADP, detected at *m/z* 426.0224, where it was most abundant in the lens and retina (Figure 4C). Interestingly, some signals were detected specifically in distinct ocular fluid compartments. Putative taurine (*m/z* 124.0070) and cystine (*m/z* 239.0165), both sulphur-containing small molecules that play a role in redox balance in the eye, were localised to the VH (Figure 4D) and AH (Figure 4E), respectively. When the irido-corneal angle region was analysed at higher spatial resolution (50 μm), this molecular compartmentalisation was also evident.

GSH, detected at *m/z* 306.0766, was localised to both humours, iris and cornea, but was most abundant in the lens (Figure 4F), while putative PS(40:6) (Figure 4G) and ADP (Figure 4H) localisations were to multiple tissues and were consistent with the low resolution analysis (c.f. Figures 4B and 4C, respectively). A signal at *m/z* 191.0193, assigned citric acid, was detected in both ocular humours (Figure 4I), and at highest abundance in the AH, while putative uric acid (*m/z* 202.9976) was found solely in the AH (Figure 4J). On-tissue MS/MS was performed to confirm identifications where possible (see *Supplemental Information*). However, some identifications remain putative, and while they are consistent with known ocular biology, they are unconfirmed since their signal level is relatively low and therefore difficult to analyse by on-tissue MS/MS.

However, to demonstrate that tandem mass spectrometry imaging experiments could be performed on the prepared whole eyeball sections to identify and map small molecule signals, the posterior eyeball of an adult black bream eye was targeted (Figure 5). The larger adult black bream eye was chosen for practical considerations, and small regions of the whole eyeball section were analysed that encompassed both tissues (choroid, retina) and ocular fluid (VH). Putative phospholipid signals at nominal *m/z* 834 were analysed using MS/MS (CID) MALDI-IMS. A wide isolation window of 10 *m/z* was utilised to optimise signal intensity. One phosphatidylethanolamine (Figure 5A) and two phosphatidylserine (Figure 5B) species were identified by matching predicted and observed CID lipid fragments (Table 2, LipidMAPS), and localised to different structures at the back of the eye. Phosphatidylethanolamine PE(22:6/22:6) was found predominantly in the choroid, with evidence of it also distributed at lower concentrations in the retina and VH (Figure 5C, *left*). The two phosphatidylserines (PS(22:6/18:0) and PS(22:5/18:1)) were localised predominantly in the retina, potentially in different retinal cell layers, and at lower concentration in the underlying muscle (Figure 5C, *middle* and *right*).

To demonstrate that the developed methodology was reproducible, every second serial section through a whole mouse eye spaced at 35 µm was taken and prepared for 3D MALDI imaging (Figure 6). A total of 47 sections were mounted onto 4 slides (Figure 6A), and data collected at 35 µm spatial resolution. To demonstrate that other MALDI matrices could be utilised, we analysed the sections using BPYN as matrix in negative ionisation mode. We were able to annotate between 160-174 metabolites for sections 18 and 19 using Metaspace matching to the HMDB, ChEBI, LipidsMaps and SwissLipids databases, from small molecule metabolites through to larger gangliosides. We were able to map distinct *m/z*'s throughout the 3D model to identify specific tissue types (Figure 6B) including a putative dipeptide PhePhe (orange, *m/z* 311.1401) to the lens core, GSH (red, *m/z* 306.0766) predominantly to the lens periphery, PS(44:12) (yellow, *m/z* 878.4977) to the retina and optic nerve bundle, a putative mass matching to a prostaglandin E (PGE, green, *m/z* 353.233) found distributed throughout the AH and VH, and surrounding tissues, and known to be expressed in the eye[54, 55]. Finally, an unknown metabolite (dark blue, *m/z* 464.3143) was found predominantly localised to the VH. Overlay of all signals demonstrates the distinct spatial distributions and in some cases co-localisation of PGE and the unknown metabolite shown as a light blue signal. To determine reproducibility across the 47 imaged sections, we generated a principal component analysis (PCA) using data from 37 annotated metabolites (Figure 6C). In this analysis, each data point in the PCA plot corresponds to a single pixel in the entire 3D data set. The data shows a high degree of section-to-section reproducibility within a single organ, indicated by the numerous intersections and large overlaps of ellipses, which represent the standard deviation for each consecutive section (95% quantile), with the majority of data points contained within. Image alignment of each serial section, then 3D rendering enables the examination of the distribution of the same molecules throughout the eye (Figure 6D). A slice through the image volume, taken in the sagittal plane to show the optical

axis, demonstrates the tissue specific localisation of each of the metabolites. For example, the localisation of GSH to the periphery of the lens tissue forming a hollow sphere delineates the highly metabolically active outer fibre cells of the lens cortex, from the older, less metabolically active nuclear fibre cells (Figure 6D ii), while the entirety of the neuronal retinal layer can be defined by the highly abundant PS(44:12) lipid species (Figure 6D iv). An additional perspective of the 3D image volume is available in the Supplemental Information (Figure S7).

Finally, to demonstrate that the method has utility at high lateral resolutions, 10 µm spatial data on equivalent mouse eye sections coated with BPYN matrix was collected on the newly released timsTOF Flex system[56]. Spatial segmentation of the resulting data (Figure 7 A and D) is able to describe all major tissues types within the eye, including cornea (epithelium and stroma), iris, lens including anterior pole epithelial cell monolayer and outer-, mid-, inner-cortical and nuclear regions, retinal layers, optic nerve bundle and choroid/sclera. Selected ions demonstrate selectivity for certain cell types. For example, putative oleic acid *m/z* 281.2498 (Figure 7B) was observed predominantly in the outer tissues of the eye (retinal pigmented epithelium, ciliary body, corneal epithelium and iris) but also in high concentrations within the cortex of the lens. Distribution within the lens cortex is consistent with prior observations of highly oleated Aquaporin-0 within other mammalian lens tissues[57]. Docosahexaenoic acid (DHA) *m/z* 327.2309 was found throughout the retina, iris, and corneal stroma but at low abundance in the lens (Figure 7C). DHA is highly abundant in retinal layers and is the major PUFA component (up to 60%)[58]. The major tissue phosphatidyl inositol PI(38:4) *m/z* 885.5497 was found predominantly confined to the photoreceptor cell layer (inner and outer segments), consistent with the functional role of PIs in rod outer segments[59], and at lower abundances throughout other tissues types (Figure 7E). The ganglioside, GM1(38:1) *m/z* 1572.9090, was detected at low abundance and localised in the inner retinal layers (nerve fibre layer

and ganglion cell layer) and optic nerve bundle, consistent with its previous detection in mammalian retinae[60, 61].

DISCUSSION

In this study, a combination of tissue section collection via adhesive cryofilm, copper foil tape mounting of cryofilm to glass slides, and freeze-drying of sections allowed the concentration gradients of small molecules in whole eye sections to be analysed by MALDI-FT-ICR IMS. While small molecules and metabolites have previously been detected in major ocular tissues, this study revealed that small molecule gradients exist in the ocular humours, particularly in the teleost eye. In addition, the relative positions of the major ocular tissues was well preserved, including tissue fine structure to the level of retinal layers (see Figures 5 and 7), albeit with some tissue cracking following freeze drying. This tissue cracking appeared to be along natural fissure lines, possibly through the disruption of cell-to-cell junctions. In comparison to the eyeballs from rat, mouse and juvenile black bream, the rabbit eye was more challenging to routinely collect sections from, requiring thicker sections (50 μm). In addition, the higher spatial resolution data sets exacerbated the visualisation areas of tissue cracking (e.g. lens tissue). Speckling of some signals from the ocular humours was also present (c.f. Figure 4E and Figure 4J). This speckling may be an artefact of the freezing/freeze-drying process of the larger eye, or of the in solution matrix spray deposition process. This suggests that while the current protocol can be applied to larger eyes, further optimisation is required. This could include, for example, matrix deposition via vacuum sublimation, possibly with subsequent recrystalisation, as an alternative matrix application technique to limit speckling from small molecules in the ocular fluids. Nevertheless, the current protocol was compatible with a range of eyeball sizes, and allowed the distributions of small molecules present in tissues and humours to be compared and the potential for ocular inter-tissue metabolism to be assessed.

One advantage of the presented approach was the use of copper foil tape to adhere the cryofilm to the target slide. Previous studies have utilised double-sided carbon tape[20], such as that used in the mounting of EM tissue sections, while a recent study in plants has also reported the use of copper foil tape to adhere tape-transferred sections to MALDI targets[23]. The carbon tape surface is not flat, and contains frequent pits of varying sizes that can create variable ion signal in a MALDI mass spectrometer due to the fixed nature of the laser focus. While the effect of this tape surface is mitigated somewhat by data normalisation and low spatial resolution sampling (i.e. ~150 μm), higher resolution sampling is likely to be compromised. The copper foil tape is considerably flatter, facilitating more consistent spectrum-to-spectrum quality and therefore better quality MALDI-IMS data. We were able to demonstrate high lateral (10 μm) resolution imaging in mouse eyes using the MALDI timsTOF Flex MS on sections mounted using this method. Presumably, non-conductive tapes that are flat could also be used in MALDI-IMS instruments with de-coupled ion sources, while conductive metal foil tapes should be used in e.g. time-of-flight instruments that require a conductive target, thus facilitating higher voltages. In this study, we were able to use non-conductive cryofilm tape due to the source of the MALDI-FT-ICR and timsTOF instruments not requiring a conductive tissue mounting surface. For those instruments that do require a conductive surface, a conductive cryofilm transfer tape[62] would be required for optimal spectral quality and consistency.

Initially, our sampling resolution was set to 50 μm, primarily due to the dimensions of the laser beam, instrument sensitivity and required acquisition time. While this allowed multiple ocular tissues, such as the retina and choroid, to be defined in the juvenile black bream eye based on unique small molecule signals present in each tissue, including multiple regions of the lens, layers of the retina that are known to contain unique small molecule signatures[39, 40] were not resolved.

MS/MS analysis of the adult black bream showed that more than one retinal cell layer could be resolved, but this was still limited in comparison to previous studies[39, 40]. This was not a limit of the cryofilm or freeze-drying process. Subsequent analysis demonstrated that we were able to resolve the retinal layers of the mouse eye on an instrument with much higher spatial resolution.

The presented protocol was compatible with different metabolite matrices (i.e. NEDC, BPYN and DHB (*data not shown*)). Other matrices could be used to expand the range of small molecules detected in the ocular humours, however they would have to be salt tolerant to avoid any tissue washing steps that would likely destroy small molecule gradients in the ocular humours. As with any MALDI imaging analysis of biological tissue, the detected distributions are a result of the choice of matrix, the ability of molecules to be ionised from a heterogeneous tissue section, and the sensitivity of the mass spectrometer. It is likely that some ions are differentially suppressed in the different regions of whole eyeball sections (c.f. tissue and humours). One way to address this is to first identify molecules of interest using tandem mass spectrometry approaches, then implement a targeted analysis using a spray-deposited stable isotopically-labelled standard approach to produce more accurate ion distributions which would account for tissue section regions and molecules prone to ion suppression.

However, one limitation that remains is the unequivocal identification of small molecule signals detected in MALDI IMS experiments. On-tissue MS/MS was successfully used to identify phospholipid signals in the posterior eye. The identification of these phospholipids in the retina was consistent with previous analysis of phospholipids in fish brain and retina tissue, where a higher degree of unsaturation of polyunsaturated fatty acids was observed.[63] However, the majority of *m/z* signals remain unidentified, particularly in the black bream potentially due to the lack of ocular

humour analysis of teleost eyes, and their identification would allow additional interpretation of their possible biological significance to be made. In the rabbit eyeball analysis, the trends of our provisionally identified ocular humour metabolite distributions were consistent with previous studies, where cystine (the more stable, oxidised form of cysteine), uric acid, and citric acid have been detected in AH at higher abundance than VH[27, 64, 65], and taurine, as an important molecule that supports retinal photoreceptor cell function, has been detected at higher levels in the VH than AH[66, 67]. Complementary orthogonal LC-MS metabolomics studies would aid greatly in identifying endogenous metabolites but are beyond the scope of this method.

Despite the spatial resolution and identification limitations, in the teleost eye a number of small molecule signals were localised in the AH either around both anterior and posterior surfaces of the iris, or primarily in the iridocorneal angle (see Figures 3M and 3N). This was in contrast to the rodent eyes where equivalent molecular distributions were not observed, suggesting that the distributions observed in the teleost eye are not an artefact of analysis. Moreover, in mammals the iridocorneal region contains the ciliary body (posterior chamber) and trabecular meshwork (anterior chamber), which circumferentially produces and drains AH, respectively. As a filtrate of the blood, AH contains hundreds of small molecules[26, 27]. In teleosts the ciliary body is absent[68], and the AH is instead produced from the posterior epithelium adjacent to the iris[69]. In zebrafish, AH has been proposed to undergo vectorial flow from the dorsal ciliary epithelium to the iridocorneal and ciliary openings of the ventral canalicular network and ventral vitreal-retinal vessels[70]. The patterns observed in the current study suggest accumulation and concentration of several small molecules in these locations, and therefore may be established or produced by this vectorial flow. This level of detail has not been reported in previous studies of the AH due to the lack of spatial information.

In the relatively smaller mouse eye, we were able to collect data at 35 µm spatial resolution on FT-ICR and at 10 µm with timsTOF. Serial sectioning and sequential collection of images enabled us to demonstrate the first 3D IMS model of the eye. Similar distributions and localisations of molecules could be observed throughout the tissues of the eye including within the AH and VH. Individual cell layers of the neural retina were not distinctly resolved at 35 µm but could be resolved at 10 µm, as has been previously demonstrated[39]. For 3D imaging, there is a significant cost in instrument time when there are requirements for both high spatial and mass resolving power. In our 3D example, approximately 5 days of continuous acquisition on the MALDI FT-ICR MS were required to collect a full set of images.

CONCLUSIONS

A highly reproducible methodology for the spatial mapping of small molecules in tissue containing fluid-filled compartments has been developed, using the example of whole eyeballs from teleost fish and common laboratory animals. The presented results suggest that a complex array of small molecule concentration gradients exist in the ocular humours of the teleost eye, and that compartmentalisation of some small molecules occurs in the ocular humours of the rabbit. In the future, this approach could be trialled with eyeballs from larger animals which more closely model the dimensions and physiology of the human eye, such as the porcine eye, to establish whether similar small molecule concentration gradients are present. This should assist in elucidating the role of these small molecules in the integrated functioning of the eye, and may also be useful for tracing the intraocular pathways and binding sites of exogenous small molecules, such as pharmaceuticals developed as ocular therapeutics. The development of 3D images in various degenerative disease models such as diabetic retinopathy and aged related macular degeneration will enable detailed examination of biochemical features and progression of disease in a spatial manner.

ACKNOWLEDGEMENTS

The authors wish to thank the University of Melbourne Dyason Fellowship programme, the Health Research Council of New Zealand (ACG), the Marsden Fund of New Zealand, the University of Auckland Mass Spectrometry Hub, and Metabolomics Australia which is supported by funds from the Australian Government's National Collaborative Research Infrastructure Scheme (NCRIS) administered through Bioplatforms Australia (BPA) Ltd. We thank J. Wilkinson-Berka, University of

Melbourne and E. Burrows, Florey Institute of Neuroscience and Mental Health, for mouse eye tissues. We thank A. Ly and J. Oetjen, Bruker Daltonik, Bremen, Germany for MALDI timsTOF data acquisition and analysis.

FIGURES

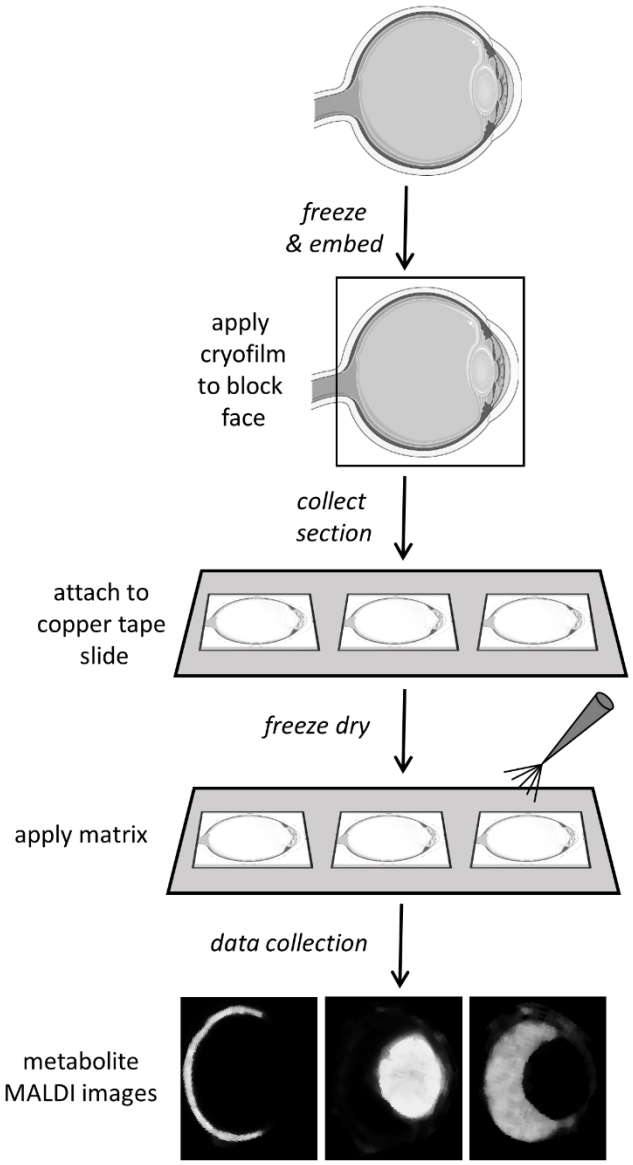

Figure 1

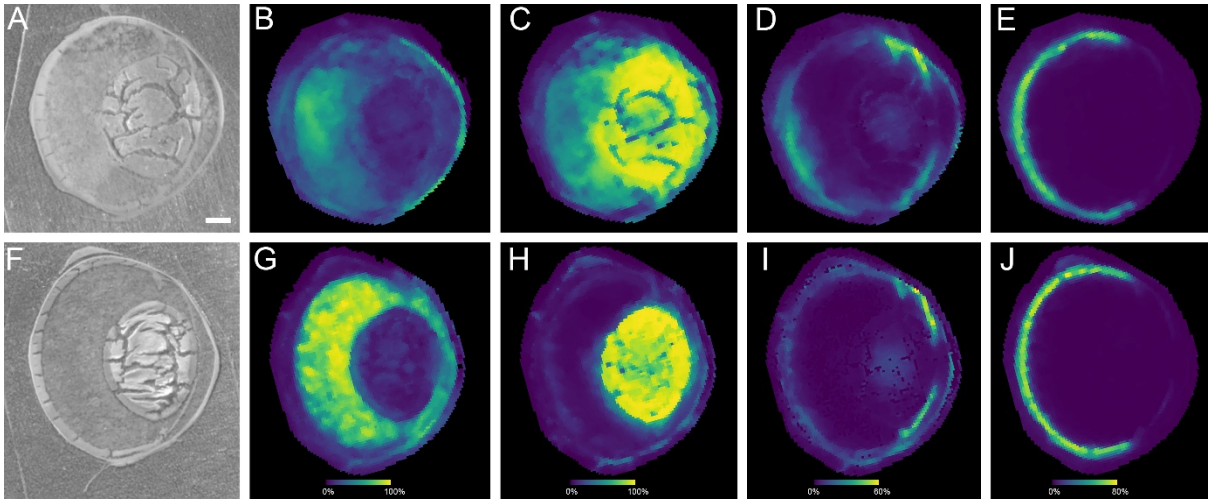

Figure 2

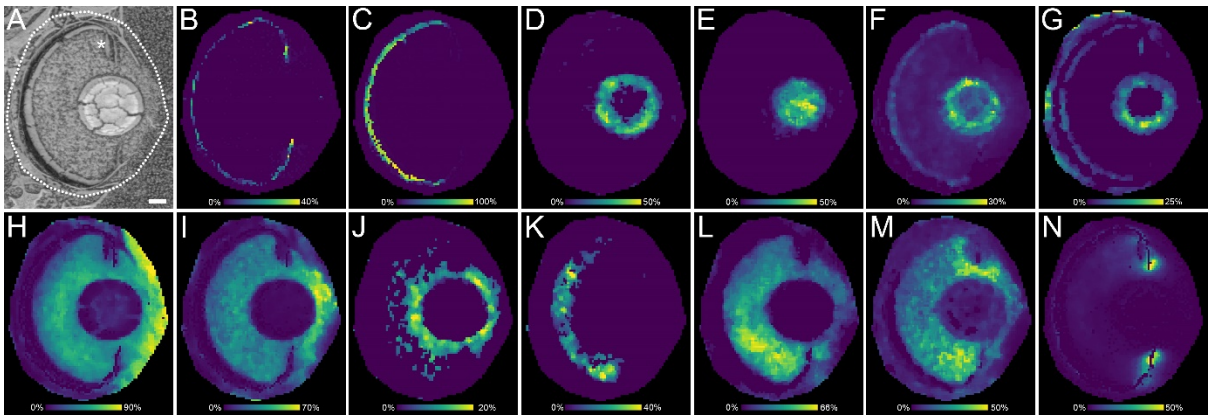

Figure 3

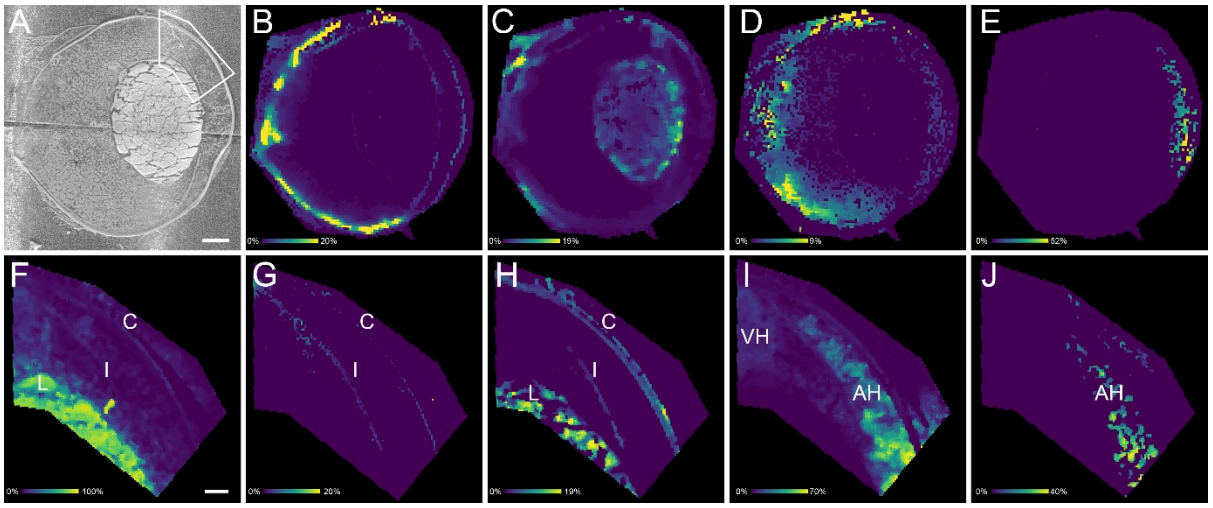

Figure 4

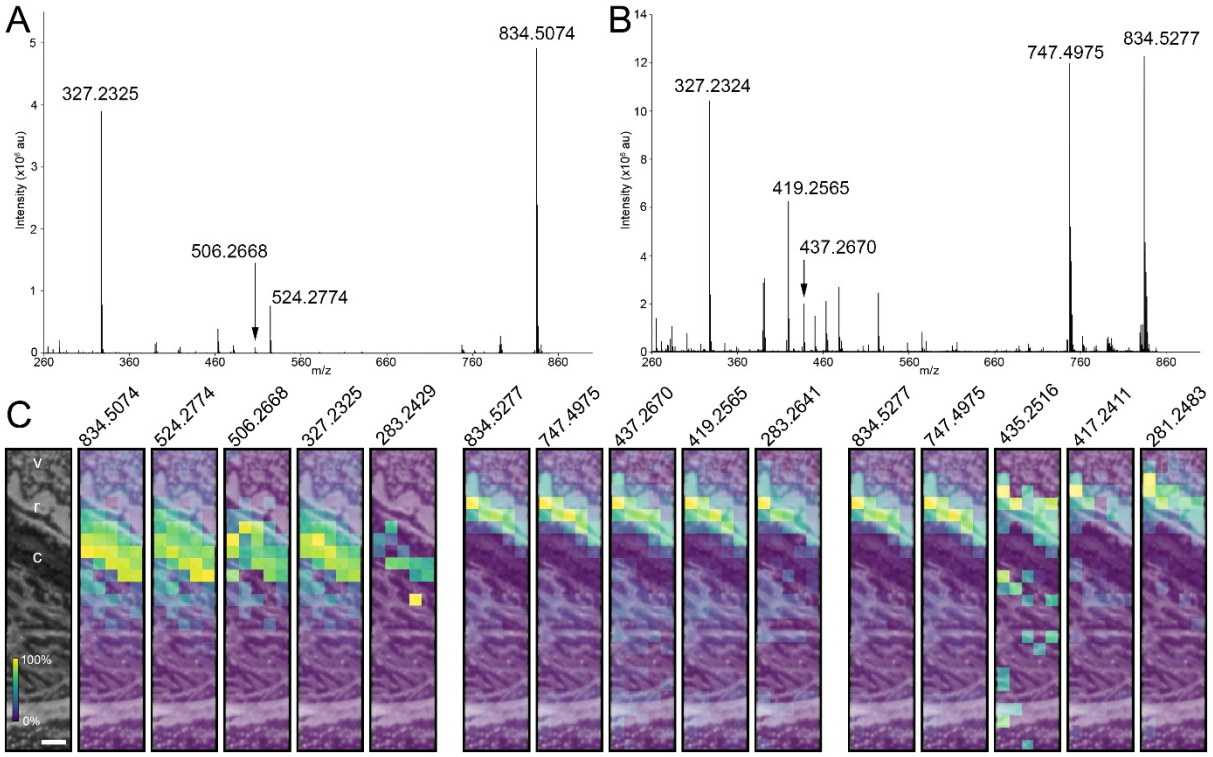

Figure 5

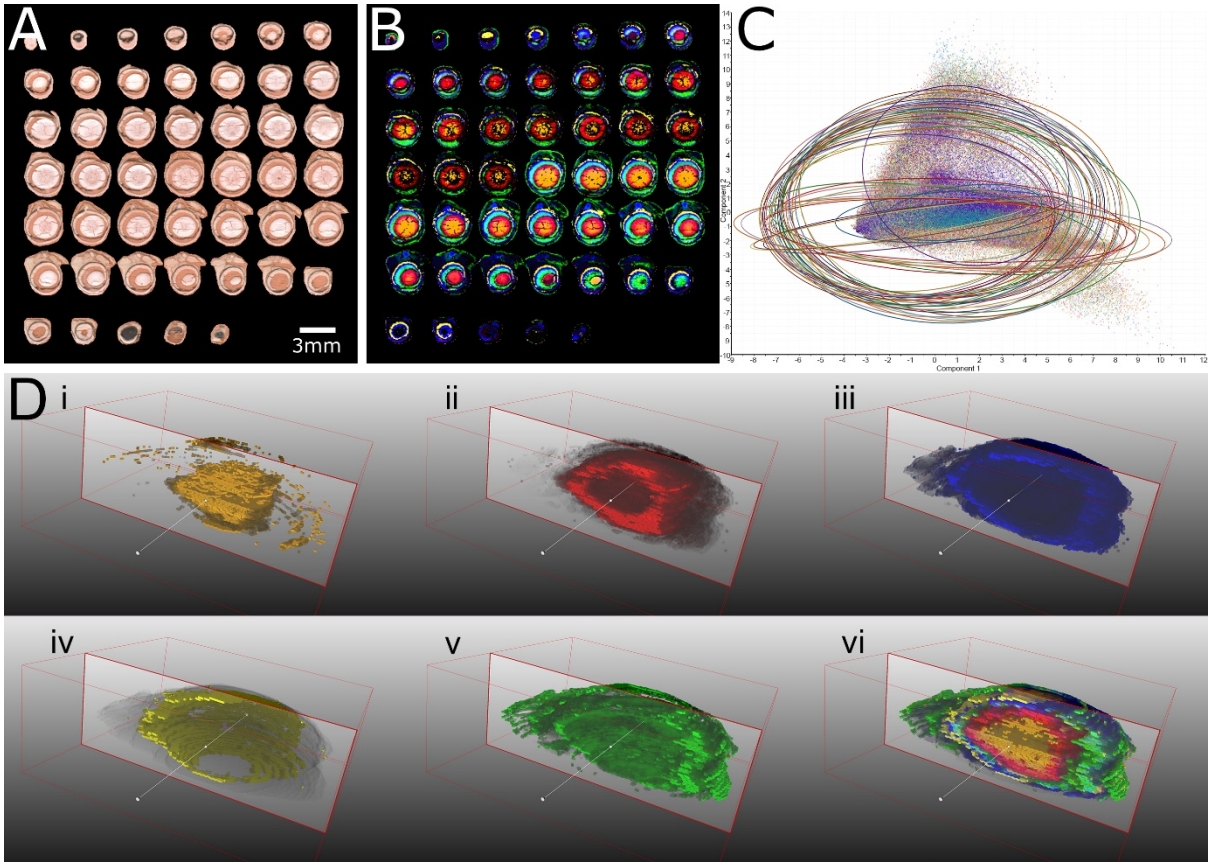

Figure 6

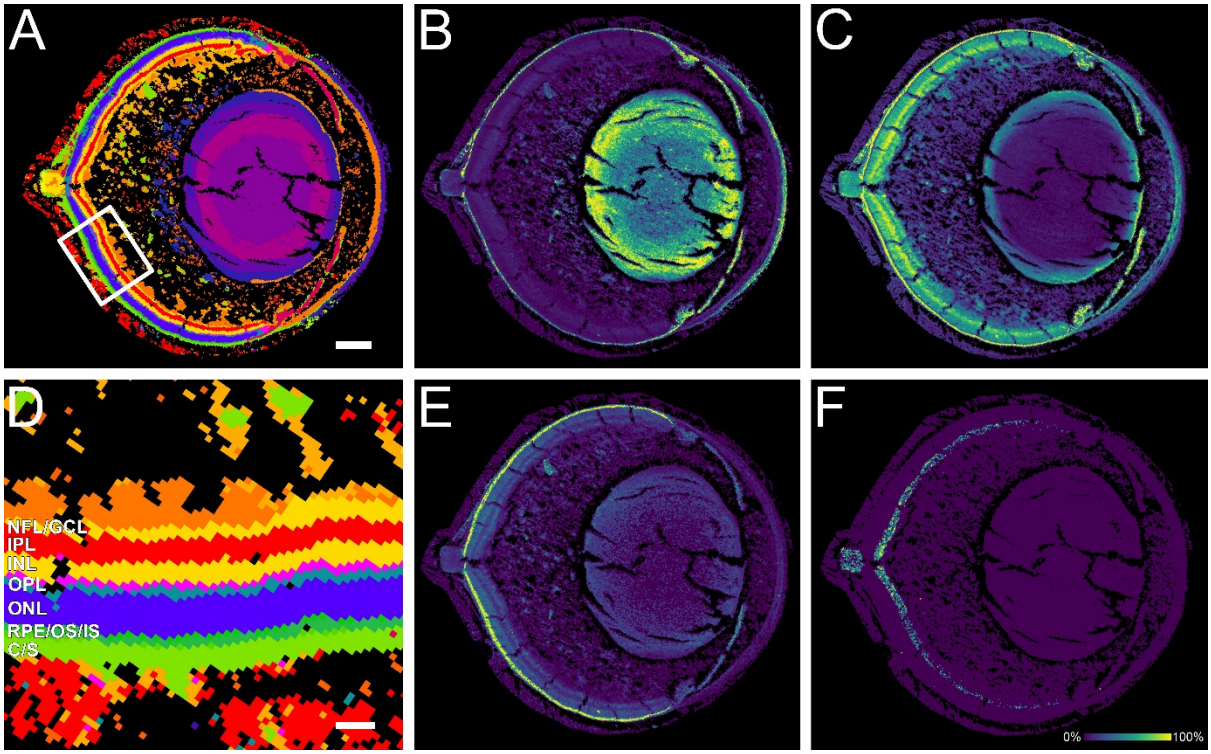

Figure 7

TABLES

Table 1: Observed and predicted *m/z* and putative identifications for ocular metabolites

Metabolite	Adduct	Observed *m/z*	Predicted *m/z*	Error (ppm)	Localisation
Mouse					
Oleic Acid	$[M-H]^-$	281.2498	281.2486	4.3	retina, lens
Glutathione*	$[M-H]^-$	306.0761	306.0754	2.3	lens
Phe-Phe	$[M-H]^-$	311.1401	311.1390	3.5	lens nucleus
DHA	$[M-H]^-$	327.2309	327.2330	6.4	retina
PGE	$[M-H]^-$	353.2330	353.2323	2.0	humours
unknown	-	464.3143	-	-	vitreous humour
PS(44:12)	$[M-H]^-$	878.4977	878.4967	1.1	retina
PI(38:4)	$[M-H]^-$	885.5497	885.5493	0.5	retina
Ganglioside GM1	$[M-H]^-$	1572.9090	1572.9007	5.3	retina
Rat					
Glucose Myo-inositol	$[M+Cl]^-$	215.0324	215.0317	3.3	vitreous humour
Glutathione*	$[M-H]^-$	306.0761	306.0754	2.3	lens
AMP*	$[M-H]^-$	346.0554	346.0547	2.0	iris
PS(40:6)*	$[M-H]^-$	834.5302	834.5291	1.3	retina
Black Bream					
N-acetyl-histidine*	$[M-H]^-$	196.0740	196.0717	11.7	lens cortex, retina
unknown	†$[M+Cl]^-$	261.9428	-	-	uvea
Glutathione*	$[M-H]^-$	306.0792	306.0754	10.1	lens
unknown	†$[M+Cl]^-$	360.9988	-	-	humour, near iris
unknown	†$[M+Cl]^-$	374.9787	-	-	aqueous humour
unknown	†$[M-H]^-$	380.0046	-	-	perilenticular
unknown	†$[M-H]^-$	385.0870	-	-	vitreous humour
unknown	†$[M-H]^-$	405.1886	-	-	cryofilm
unknown	†$[M+Cl]^-$	411.9880	-	-	vitreous humour
ADP	$[M-H]^-$	426.0256	426.0210	8.2	lens cortex, retina
unknown	†$[M-H]^-$	438.1429	-	-	lens cortex
unknown	†$[M-H]^-$	504.0363	-	-	humour, near ciliary body
PS(40:6)*	$[M-H]^-$	834.5264	834.5291	3.2	retina
unknown	†$[M-H]^-$	902.4642			lens nucleus
Rabbit					
Taurine	$[M-H]^-$	124.0069	124.0063	4.8	vitreous humour
Citric acid*	$[M-H]^-$	191.0193	191.0186	3.7	aqueous humour
Uric Acid	$[M+Cl]^-$	202.9976	202.9966	4.9	aqueous humour
Cystine	$[M-H]^-$	239.0165	239.0155	4.2	aqueous humour

Glutathione*	$[M-H]^-$	306.0766	306.0754	3.9	lens
ADP*	$[M-H]^-$	426.0224	426.0210	3.3	lens, cornea
PS(40:6)*	$[M-H]^-$	834.5365	834.5291	8.9	retina

* confirmed by on-tissue MS/MS, † putative adduct

Table 2: Ions detected in MS/MS MALDI-IMS analysis of adult black bream posterior eye

Lipid	Observed *m/z* $[M-H]^-$	Predicted *m/z* $[M-H]^-$	Error (ppm)	Description
PE(22:6/22:6)	834.5074	834.5079	0.60	Precursor
	524.2774	524.2783	1.72	Loss of sn1/sn2 acyl chain
	506.2668	506.2677	1.78	Neutral loss of sn1/sn2 RCOOH group
	327.2325	327.2330	1.53	sn1/sn2 $RCOO^-$
	283.2429	283.2431	0.71	Loss of CO2 from sn1/sn2 $RCOO^-$
PS(22:6/18:0)	834.5277	834.5291	1.68	Precursor
	747.4975	747.4970	0.67	Loss of serine
	437.2670	437.2674	0.91	Loss of sn1 acyl chain and serine
	419.2565	419.2568	0.72	Neutral loss of sn1 RCOOH group and serine
	283.2641	283.2643	0.71	sn2 $RCOO^-$ ion
PS(22:5/18:1)	834.5277	834.5291	1.68	Precursor
	747.4975	747.4970	0.67	Loss of serine
	435.2516	435.2517	0.23	Loss of sn2 acyl chain as ketene and serine
	417.2411	417.2412	0.24	Neutral loss of sn2 RCOOH group and serine
	281.2483	281.2486	1.07	sn1 $RCOO^-$

FIGURE LEGENDS

Figure 1. Schematic diagram of whole eye sectioning and MALDI-IMS protocol.

Figure 2. Freeze-drying of sections maintains spatial integrity of ocular metabolites. Optical scans of rat eyeball section following (A) drying at room temperature, and (F) freeze-drying. MALDI images of metabolites localised to vitreous humour (*m/z* 215.0324, B and G), lens (*m/z* 306.0761, C and H), iris (*m/z* 346.0554, D and I), and retina (*m/z* 834.5302, E and J), are delocalised in tissue sections dried at room temperature (B-E) in comparison to freeze-dried tissue (G-J). Intensity scaling is indicated below each set of MALDI images. Scale bar = 600μm.

Figure 3. MALDI images of the juvenile black bream eye. (A) Optical scan of the fish eye section prepared for MALDI-IMS. Representative MALDI images from ocular tissue - (B) uvea (*m/z* 261.9428), (C) retina (*m/z* 834.5264), (D) lens cortex (*m/z* 438.1429), (E) lens nucleus (*m/z* 902.4642), (F) lens and retina (*m/z* 196.0740) and (G) multiple tissues (*m/z* 426.0256). MALDI images were also generated from – (H) cryofilm (*m/z* 405.1886) and the ocular fluids (I) aqueous enriched (*m/z* 374.9787), (J) around the lens (*m/z* 380.0046), (K) vitreous proximal to the retina (*m/z* 411.9880), (L) vitreous (*m/z* 385.0870), (M) near the iris (*m/z* 360.9988) and (N) ciliary body (*m/z* 504.0363). Intensity scaling is indicated below each MALDI image. Asterisk = suspensory ligament. Scale bar = 4-00um.

Figure 4. Small molecule concentration gradients are present in the New Zealand white rabbit ocular fluids. (A) Optical scan of a rabbit eye section prepared for MALDI-IMS. Representative MALDI images from ocular tissue - (B) predominantly retina (*m/z* 834.5365), (C) multiple tissues (*m/z* 426.0224), and the (D) vitreous (*m/z* 124.0069) and (E) aqueous (*m/z* 239.0165) humours. MALDI images from the regions marked in panel A show (F) GSH (*m/z* 306.0766), (G) phospholipid (*m/z* 834.5365), (H) putative ADP (*m/z* 426.0223), (I) putative citric acid signal predominantly in the aqueous humour (*m/z* 191.0193) and (J) putative uric acid in the aqueous humour only (*m/z* 202.9976). Intensity scaling is indicated below each MALDI image. Scale bars = 2 mm (A–E), 600 μm (F–J). L = lens, I = iris, C = cornea, VH = vitreous humour, AH = aqueous humour.

Figure 5. Identification and localisation of lipid signals in the adult black bream eye. MS/MS spectra identifying phospholipids (A) PE(22:6/22:6) and (B) PS(40:6) detected at the back of the black bream eye. (C, *left*) MS/MS MALDI images of PE(22:6/22:6) indicated it was localised predominantly in the choroid (c) with some signal also detected in the retina (r) and vitreous humour (v). MS/MS MALDI images showed that PS(40:6) was localised predominantly in the retina, and showed that both PS(22:6/18:0) (C, *middle*) and PS(22:5/18:1) (C, *right*) were present, possibly in different retinal layers. All MALDI images scaled 0–100%. Scale bar = 200 μm.

Figure 6. Reproducibility of whole eyeball MALDI-IMS: Mouse eye metabolic mapping in three dimensions. (A) Optical scan of all tissue sections prepared for MALDI-IMS analysis. (B) Multi-signal MALDI images of sections, including putative dipeptide PhePhe (*m/z* 311.1401, orange), GSH (*m/z*

306.0766, red), unknown metabolite (*m/z* 464.3143, dark blue), PS(44:12) (*m/z* 878.4977, yellow), and putative prostaglandin E (PGE, *m/z* 353.2330, green), all MALDI images scale 0–100%. (C) A principal component analysis showing component 1 (*x*-axis) vs component 2 (*y*-axis), derived from 37 annotated metabolites across all 47 sections. Coloured ellipses and data points correspond to individual metabolites and represent the 95% quantile. (D) 3D volume renderings (i-vi) of the signals presented in panel B. The image volume is sliced parallel to the optical axis and orientated such that the anterior eye is to the right, and posterior eye to the left.

Figure 7. High Lateral Resolution: MALDI timsTOF image of mouse eye section acquired at 10 µm lateral resolution. (A) Unsupervised Segmentation map with clustering based on similarity. Segmentation is able to describe all major tissue types including Cornea (epithelium and stroma), Iris, Epithelial layer of the lens anterior pole, Outer-, Mid-, Inner-cortical and Nuclear regions of the lens, Retinal Layers, Optic nerve bundle and Sclera. Scale Bar = 3000 µm. Dotted box represents zoomed area in panel D. (B) Oleic acid m/z 281.2498 (annotation from metaspace) localised predominantly to the retinal pigmented epithelium, iris, corneal epithelium, and lens cortex. (C) Docosahexaenoic acid (m/z 327.2309) was more widely distributed in the retina, and in the lens outer cortex, iris, and corneal stroma. (D) Zoomed region of the segmentation map displaying several tentatively-assigned retinal layers. Scale bar = 60 µm. (E) Phosphatidyl inositol PI(38:4) (m/z 885.5497), localised predominantly to the photoreceptor inner and outer segments. (F) Ganglioside GM1(38:1) (m/z 1572.9090) localised to the nerve fibre layer of the retina. All MALDI images were scaled 0-100%. NFL = nerve fibre layer, GCL = ganglion cell layer, IPL = inner plexiform layer, INL = inner nuclear layer, OPL = outer plexiform layer, ONL = outer nuclear layer, RPE = retinal pigmented

epithelium, OS = photoreceptor outer segments, IS = photoreceptor inner segments, C = choroid, S = sclera.

REFERENCES

1. Caprioli RM, Farmer TB, Gile J. Molecular Imaging of Biological Samples: Localization of Peptides and Proteins Using MALDI-TOF MS. *Analytical Chemistry* 1997;69:4751-4760.
2. Cornett DS, Frappier SL, Caprioli RM. MALDI-FTICR Imaging Mass Spectrometry of Drugs and Metabolites in Tissue. *Analytical Chemistry* 2008;80:5648–5653.
3. DeKeyser SS, Kutz-Naber KK, Schmidt JJ, Barrett-Wilt GA, Li L. Imaging mass spectrometry of neuropeptides in decapod crustacean neuronal tissues. *Journal of Proteome Research* 2007;6:1782–1791.
4. Powers TW, Jones EE, Betesh LR, et al. Matrix assisted laser desorption ionization imaging mass spectrometry workflow for spatial profiling analysis of N-linked glycan expression in tissues. *Analytical Chemistry* 2013;85:9799-9806.
5. Reyzer M, Hsieh Y, Ng K, Korfmacher WA, Caprioli RM. Direct Analysis of Drug Candidates in Tissue by Matrix-Assisted Laser Desorption/Ionization Mass Spectrometry. *Journal of Mass Spectrometry* 2003;38:1081-1092.
6. Stoeckli M, Chaurand P, Hallahan DE, Caprioli RM. Imaging Mass Spectrometry: A New Technology for the Analysis of Protein Expression in Mammalian Tissues. *Nature Medicine* 2001;7:493-496.
7. Woods AS, Jackson SN. Brain tissue lipidomics: direct probing using matrix-assisted laser desorption/ionization mass spectrometry. *AAPS Journal* 2006;8:E391-395.
8. Kakuda N, Miyasaka T, Iwasaki N, et al. Distinct deposition of amyloid-β species in brains with Alzheimer's disease pathology visualized with MALDI imaging mass spectrometry. *Acta Neuorpathologica Communications* 2017;5:73.
9. Schwartz SA, Reyzer ML, Caprioli RM. Direct tissue analysis using matrix-assisted laser desorption/ionization mass spectrometry: practical aspects of sample preparation. *Journal of Mass Spectrometry* 2003;38:699-708.
10. Khatib-Shahidi S, Andersson M, Herman JL, Gillespie TA, Caprioli RM. Direct Molecular Analysis of Whole-Body Animal Tissue Sections by Imaging MALDI Mass Spectrometry. *Analytical Chemistry* 2006;78:6448-6456.
11. Altelaar AF, van Minnen J, Jiménez CR, Heeren RMA, Piersma SR. Direct molecular imaging of Lymnaea stagnalis nervous tissue at subcellular spatial resolution by mass spectrometry. *Analytical Chemistry* 2005;77:735-741.
12. Takai N, Tanaka Y, Inazawa K, Saji H. Quantitative analysis of pharmaceutical drug distribution in multiple organs by imaging mass spectrometry. *Rapid Communications in Mass Spectrometry* 2012;26:1549-1556.
13. Drake RR, West CA, Mehta AS, Angel PM. MALDI Mass Spectrometry Imaging of N-Linked Glycans in Tissues. *Advances in Experimental Medicine and Biology* 2018;1104:59-76.
14. Everest-Dass AV, Briggs MT, Kaur G, Oehler MK, Hoffmann P, Packer NH. N-glycan MALDI Imaging Mass Spectrometry on Formalin-Fixed Paraffin-Embedded Tissue Enables the Delineation of Ovarian Cancer Tissues. *Molecular and Cellular Proteomics* 2016;15:3003-3016.
15. Carter CL, McLeod CW, Bunch J. Imaging of phospholipids in formalin fixed rat brain sections by matrix assisted laser desorption/ionization mass spectrometry. *Journal of the American Society for Mass Spectrometry* 2011;22:1991-1998.

16. Angel PM, Norris-Caneda K, Drake RR. In Situ Imaging of Tryptic Peptides by MALDI Imaging Mass Spectrometry Using Fresh-Frozen or Formalin-Fixed, Paraffin-Embedded Tissue. *Current Protocols in Protein Science* 2018;94:e65.
17. Lemaire R, Desmons A, Tabet JC, Day R, Salzet M, Fournier I. Direct analysis and MALDI imaging of formalin-fixed, paraffin-embedded tissue sections. *Journal of Proteome Research* 2007;6:1295-1305.
18. Ly A, Buck A, Balluff B, et al. High-mass-resolution MALDI mass spectrometry imaging of metabolites from formalin-fixed paraffin-embedded tissue. *Nature Protocols* 2016;11:1428-1443.
19. Han J, Schey KL. MALDI tissue imaging of ocular lens alpha-crystallin. *Investigative Ophthalmology and Visual Science* 2006;47:2990-2996.
20. Anderson DM, Floyd KA, Barnes S, et al. A method to prevent protein delocalization in imaging mass spectrometry of non-adherent tissues: application to small vertebrate lens imaging. *Analytical and Bioanalytical Chemistry* 2015;407:2311-2320.
21. Kawamoto T. Use of a new adhesive film for the preparation of multi-purpose fresh-frozen sections from hard tissues, whole-animals, insects and plants. *Archives of Histology and Cytology* 2003;66:123-143.
22. Boughton BA, Thinagaran D. Mass Spectrometry Imaging (MSI) for Plant Metabolomics. In: Anonio C (ed), *Plant Metabolomics: Methods and Protocols, Methods in Molecular Biology*: Springer Science+Business Media, LLC, part of Springer Nature; 2018:241-252.
23. Nakabayashi R, Hashimoto K, Toyooka K, Saito K. Keeping the shape of plant tissue for visualizing metabolite features in segmentation and correlation analysis of imaging mass spectrometry in Asparagus officinalis. *Metabolomics* 2019;15:24.
24. Rosa MF, Scano P, Noto A, et al. Monitoring the Modifications of the Vitreous Humor Metabolite Profile after Death: An Animal Model. *BioMed Research International* 2015;2015:Article ID 627201.
25. Young SP, Nessim M, Falciani F, et al. Metabolomic analysis of human vitreous humor differentiates ocular inflammatory disease. *Molecular Vision* 2009;15:1210-1217.
26. Ji Y, Rao J, Rong X, Lou S, Zheng Z, Lu Y. Metabolic characterization of human aqueous humor in relation to high myopia. *Experimental Eye Research* 2017;159:147-155.
27. Pietrowska K, Dmuchowska DA, Samczuk P, et al. LC-MS-Based Metabolic Fingerprinting of Aqueous Humor. *Journal of Analytical Methods in Chemistry* 2017;2017:Article ID 6745932.
28. Grey AC, Schey KL. Age-related changes in the spatial distribution of human lens α-crystallin products by MALDI imaging mass spectrometry. *Investigative Ophthalmology and Visual Science* 2009;50:4319-4329.
29. Ronci M., Sharma S., Chataway T., et al. MALDI-MS-imaging of whole human lens capsule. *Journal of Proteome Research* 2011;10:3522-3529.
30. Ronci M., Sharma S., Martin S., Craig J.E., N.H. V. MALDI MS imaging analysis of apolipoprotein E and lysyl oxidase-like 1 in human lens capsules affected by pseudoexfoliation syndrome. *Journal of Proteomics* 2013;82:27-34.
31. Grey AC, Schey KL. Distribution of bovine and rabbit lens alpha-crystallin products by MALDI imaging mass spectrometry. *Molecular Vision* 2008;14:171-179.
32. Su SP, McArthur JD, Andrew Aquilina J. Localization of low molecular weight crystallin peptides in the aging human lens using a MALDI mass spectrometry imaging approach. *Experimental Eye Research* 2010;91:97-103.

33. Le CH, Han J, Borchers CH. Dithranol as a MALDI matrix for tissue imaging of lipids by Fourier transform ion cyclotron resonance mass spectrometry. *Analytical Chemistry* 2012;84:8391-8398.
34. Pol J, Faltyskova H, Krasny L, et al. Age-related changes in the lateral lipid distribution in a human lens described by mass spectrometry imaging. *European Journal of Mass Spectrometry* 2015;21:297-303.
35. Vidová V, Pól J, Volný M, et al. Visualizing spatial lipid distribution in porcine lens by MALDI imaging high-resolution mass spectrometry. *Journal of Lipid Research* 2010;51:2295-2302.
36. Grey AC, Demarais NJ, West BJ, Donaldson PJ. A quantitative map of glutathione in the aging human lens. *International Journal of Mass Spectrometry* 2017.
37. Nye-Wood MG, Spraggins JM, Caprioli RM, Schey KL, Donaldson PJ, Grey AC. Spatial distributions of glutathione and its endogenous conjugates in normal bovine lens and a model of lens aging. *Experimental Eye Research* 2016;154:70-78.
38. Demarais NJ, Donaldson PJ, Grey AC. Age-related spatial differences of human lens UV filters revealed by negative ion mode MALDI imaging mass spectrometry. *Experimental Eye Research* 2019;184.
39. Anderson DMG, Ablonczy Z, Koutalos Y, et al. High Resolution MALDI Imaging Mass Spectrometry of Retinal Tissue Lipids. *Journal of The American Society for Mass Spectrometry* 2014;25:1394-1403.
40. Zemski Berry KA, Gordon WC, Murphy RC, Bazan NG. Spatial organization of lipids in the human retina and optic nerve by MALDI imaging mass spectrometry. *Journal of Lipid Research* 2014;55:504-515.
41. Ablonczy Z, Higbee D, Anderson DM, et al. Lack of correlation between the spatial distribution of A2E and lipofuscin fluorescence in the human retinal pigment epithelium. *Investigative Ophthalmology and Visual Science* 2013;54:5535-5542.
42. Ablonczy Z, Higbee D, Grey AC, Koutalos Y, Schey KL, Crouch RK. Similar molecules spatially correlate with lipofuscin and N-retinylidene-N-retinylethanolamine in the mouse but not in the human retinal pigment epithelium. *Archives of Biochemistry and Biophysics* 2013;539:196-202.
43. Grey AC, Crouch RK, Koutalos Y, Schey KL, Ablonczy Z. Spatial Localization of A2E in the Retinal Pigment Epithelium. *Investigative Ophthalmology and Visual Science* 2011;52:3926-3933.
44. Anderson DM, Ablonczy Z, Koutalos Y, et al. Bis(monoacylglycero)phosphate lipids in the retinal pigment epithelium implicate lysosomal/endosomal dysfunction in a model of Stargardt disease and human retinas. *Scientific Reports* 2017;7:17352.
45. Palmer AD, Griffiths R, Styles I, Claridge E, Calcagni A, Bunch J. Sucrose cryo-protection facilitates imaging of whole eye sections by MALDI mass spectrometry. *Journal of Mass Spectrometry* 2012;47:237-241.
46. Nakashima Y, Setou M. Distribution of Antisense Oligonucleotides in Rat Eyeballs Using MALDI Imaging Mass Spectrometry. *Mass Spectrometry* 2018;7:A0070.
47. Groseclose MR, Castellino S. An Investigation into Retigabine (Ezogabine) Associated Dyspigmentation in Rat Eyes by MALDI Imaging Mass Spectrometry. *Chemical Research in Toxicology* 2019;32:294-303.
48. Grove KJ, Kansara V, Prentiss M, et al. Application of Imaging Mass Spectrometry to Assess Ocular Drug Transit. *SLAS Discovery* 2017;22:1239-1245.
49. Mori N, Mochizuki T, Yamazaki F, et al. MALDI imaging mass spectrometry revealed atropine distribution in the ocular tissues and its transit from anterior to posterior regions in the whole-eye of rabbit after topical administration. *PLoS One* 2019;14:e0211376.

50. Brignole-Baudouin F, Desbenoit N, Hamm G, et al. A New Safety Concern for Glaucoma Treatment Demonstrated by Mass Spectrometry Imaging of Benzalkonium Chloride Distribution in the Eye, an Experimental Study in Rabbits. *PLoS One* 2012;7:e50180.
51. Palmer A, Phapale P, Chernyavsky I, et al. FDR-controlled metabolite annotation for high-resolution imaging mass spectrometry. *Nature Methods* 2017;14:57-60.
52. Bruinen AL, van Oevelen C, Eijkel GB, Van Heerden M, Cuyckens F, Heeren RM. Mass Spectrometry Imaging of Drug Related Crystal-Like Structures in Formalin-Fixed Frozen and Paraffin-Embedded Rabbit Kidney Tissue Sections. *Journal of the American Society for Mass Spectrometry* 2016;27:117-123.
53. Buck A, Ly A, Balluff B, et al. High-resolution MALDI-FT-ICR MS imaging for the analysis of metabolites from formalin-fixed paraffin-embedded clinical tissue sample. *Journal of Pathology* 2015;237:123-132.
54. Doucette LP, Walter MA. Prostaglandins in the eye: Function, expression, and roles in glaucoma. *Ophthalmic Genetics* 2017;38:108-116.
55. Goh Y, Urade Y, Fujimoto N, Hayaishi O. Content and formation of prostaglandins and distribution of prostaglandin-related enzyme activities in the rat ocular system. *Biochimica et Biophysica Acta* 1987;921:302-311.
56. Spraggins JM, Djambazova KV, Rivera ES, et al. High performance molecular imaging with MALDI trapped ion mobility time-of-flight (timsTOF) mass spectrometry. *ChemRxiv* 2019;9210059.
57. Schey KL, Guttierrez DB, Wang Z, Wei J, Grey AC. Novel fatty acid acylation of lens integral membrane protein aquaporin-0. *Biochemistry* 2010;49:9858-9865.
58. Fliesler SJ, Anderson RE. Chemistry and metabolism of lipids in the vertebrate retina. *Progress in Lipid Research* 1983;22:79-131.
59. Rajala RVS, Rajala A, Morris AJ, Anderson RE. Phosphoinositides: Minor lipids make a major impact on photoreceptor cell functions. *Scientific Reports* 2014;4:5463.
60. Daniotti JL, Landa CA, Gravotta D, Maccioni HJF. GD3 ganglioside is prevalent in fully differentiated neurons from rat retina. *Journal of Neuroscience Research* 1990;26:436-446.
61. Dreyfus H, Guérold B, Fontaine V, Sahel J, Hicks D. Simplified ganglioside composition of photoreceptors compared to other retinal neurons. *Investigative Ophthalmology and Visual Science* 1996;37:574-585.
62. Saigusa D, Saito R, Kawamoto K, et al. Conductive Adhesive Film Expands the Utility of Matrix-Assisted Laser Desorption/Ionization Mass Spectrometry Imaging. *Analytical Chemistry* 2019;epub ahead of print.
63. Tocher DR, Harvie DG. Fatty acid compositions of the major phosphoglycerides from fish neural tissues; (n−3) and (n−6) polyunsaturated fatty acids in rainbow trout (Salmo gairdneri) and cod (Gadus morhua) brains and retinas. *Fish Physiology and Biochemistry* 1988;5:229-239.
64. Kunikata H, Ida T, Sato K, et al. Metabolomic profiling of reactive persulfides and polysulfides in the aqueous and vitreous humors. *Scientific Reports* 2017;7:41984.
65. Picher SP, Rose RC. Water soluble antioxidants in mammalian aqueous humor: interaction with UV B and hydrogen peroxide. *Vision Research* 1998;38:2881-2888.
66. Girela E, Villanueva E, Irigoyen P, Girela V, Hernández-Cueto C, Peinado JM. Free amino acid concentrations in vitreous humor and cerebrospinal fluid in relation to the cause of death and postmortem interval. *Journal of Forensic Science* 2008;53:730-733.
67. Heinämäki AA, Muhonen AS, Piha RS. Taurine and other free amino acids in the retina, vitreous, lens, iris-ciliary body, and cornea of the rat eye. *Neurochemical Research* 1986;11:535-542.

68. Copeland DE. The Anatomy and Fine Structure of the Eye in Fish. VI Ciliary Type Tissue in Nine Species of Teleosts. *Biological Bulletin* 1982;163:131-143.
69. Zadunaisky J. The Electrolyte Content, Osmolarity and Site of Sectretion of the Aqueous Humour in Two Teleost Fishes (*Carassius auratus* and *Diplodus sargus*). *Experimental Eye Research* 1972;14:99-110.
70. Gray MP, Smith RS, Soules KA, John SWM, Link BA. The aqueous humor outflow pathway of zebrafish. *Investigative Ophthalmology and Visual Science* 2009;50:1515-1521.

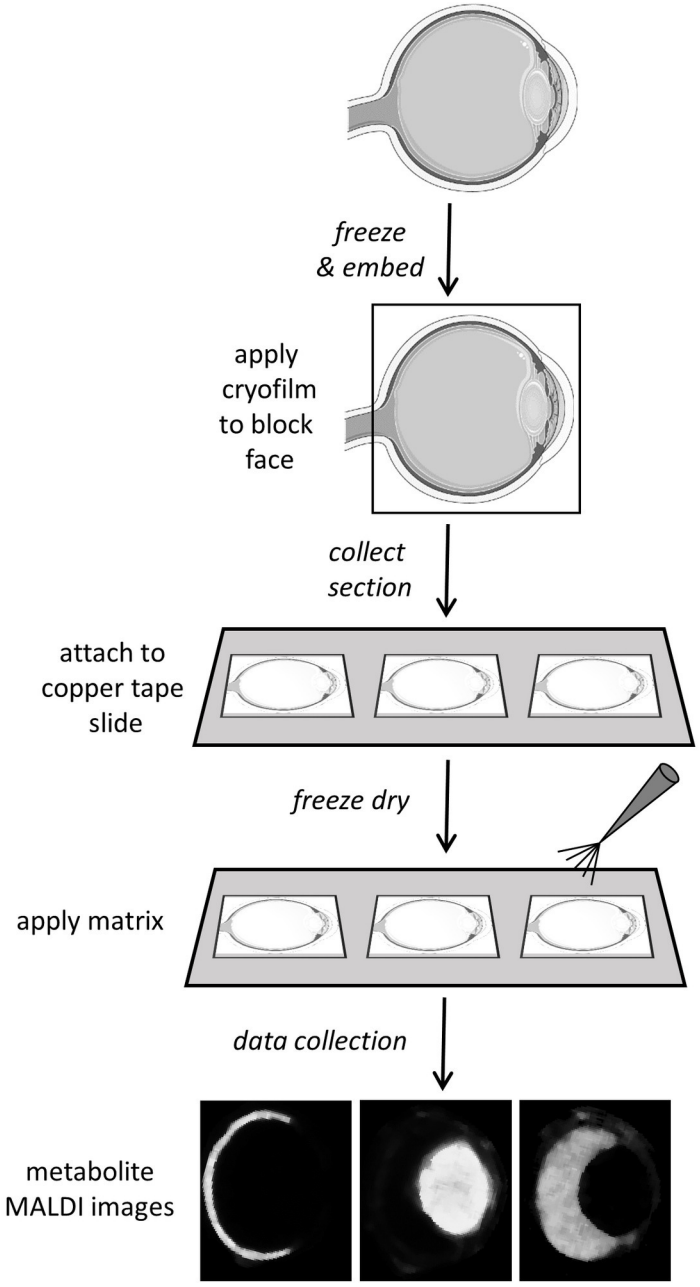

JMS_4460_Figure 1.jpg

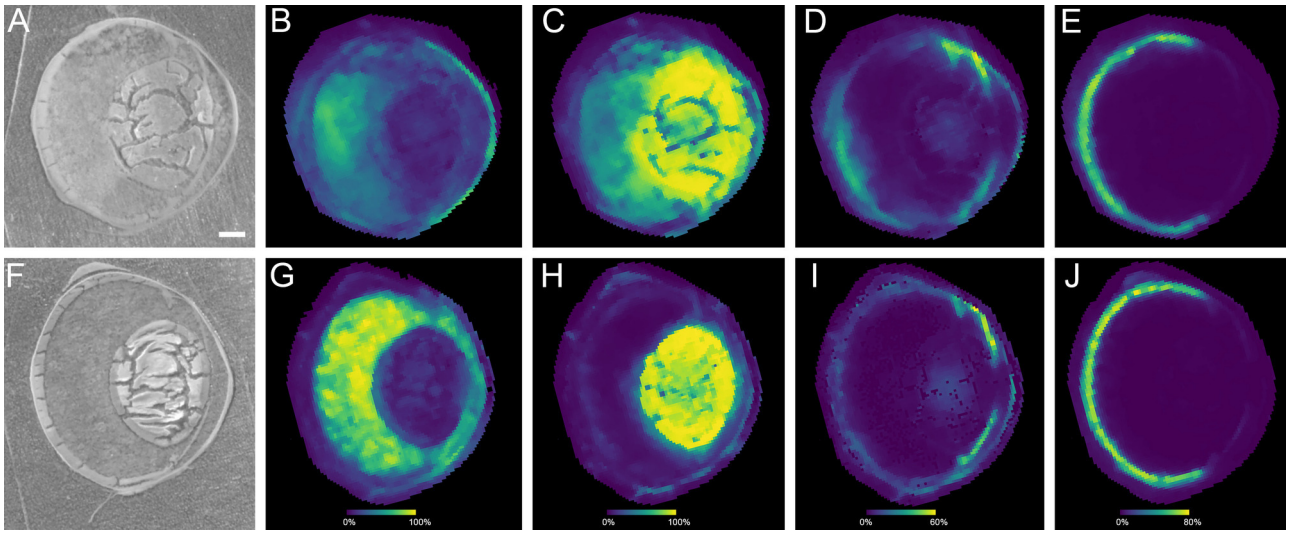

JMS_4460_Figure 2.jpg

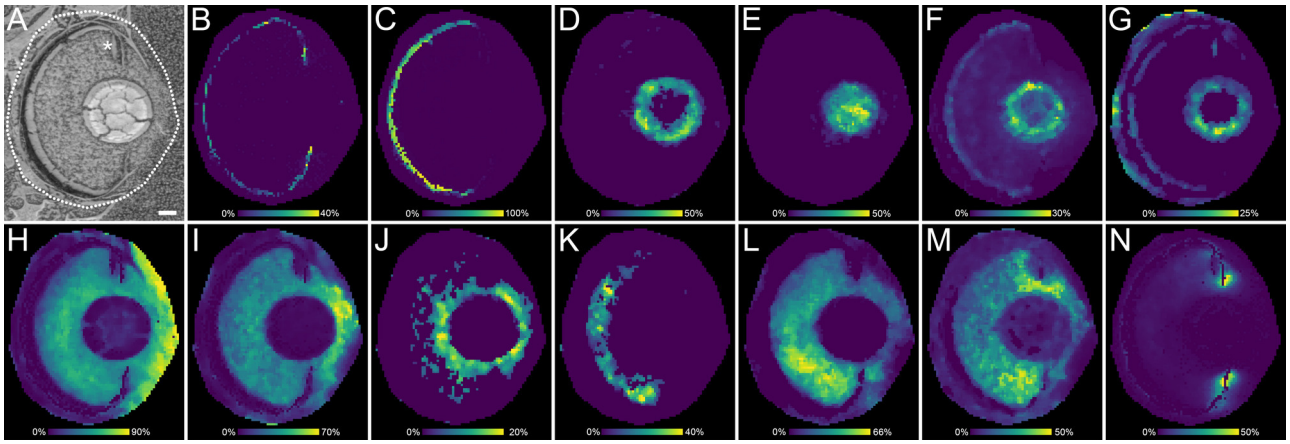

JMS_4460_Figure 3.jpg

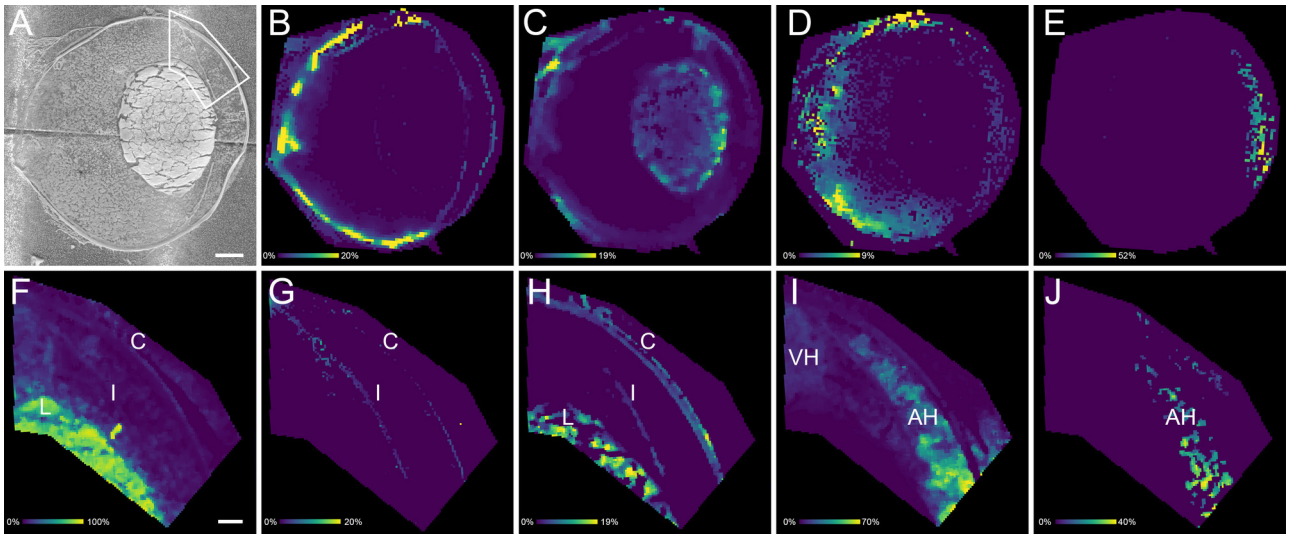

JMS_4460_Figure 4.jpg

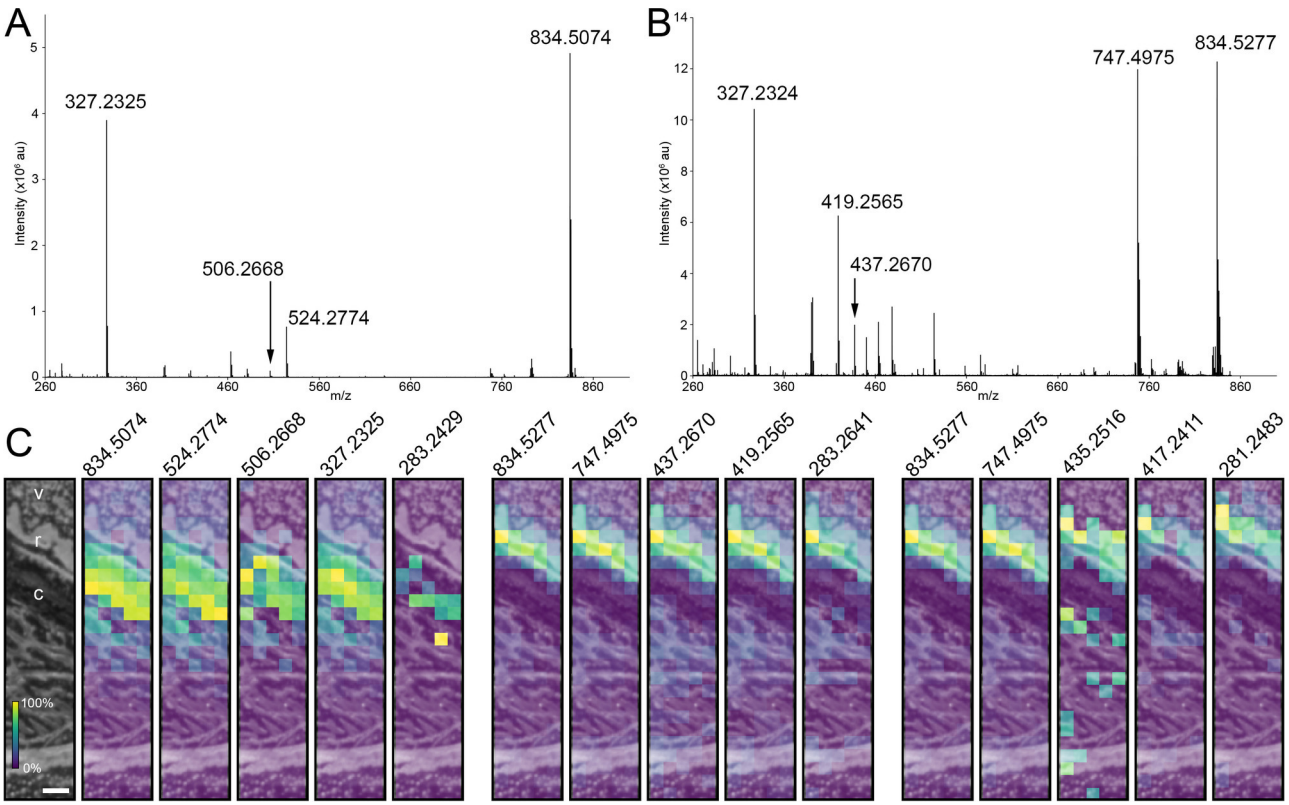

JMS_4460_Figure 5.jpg

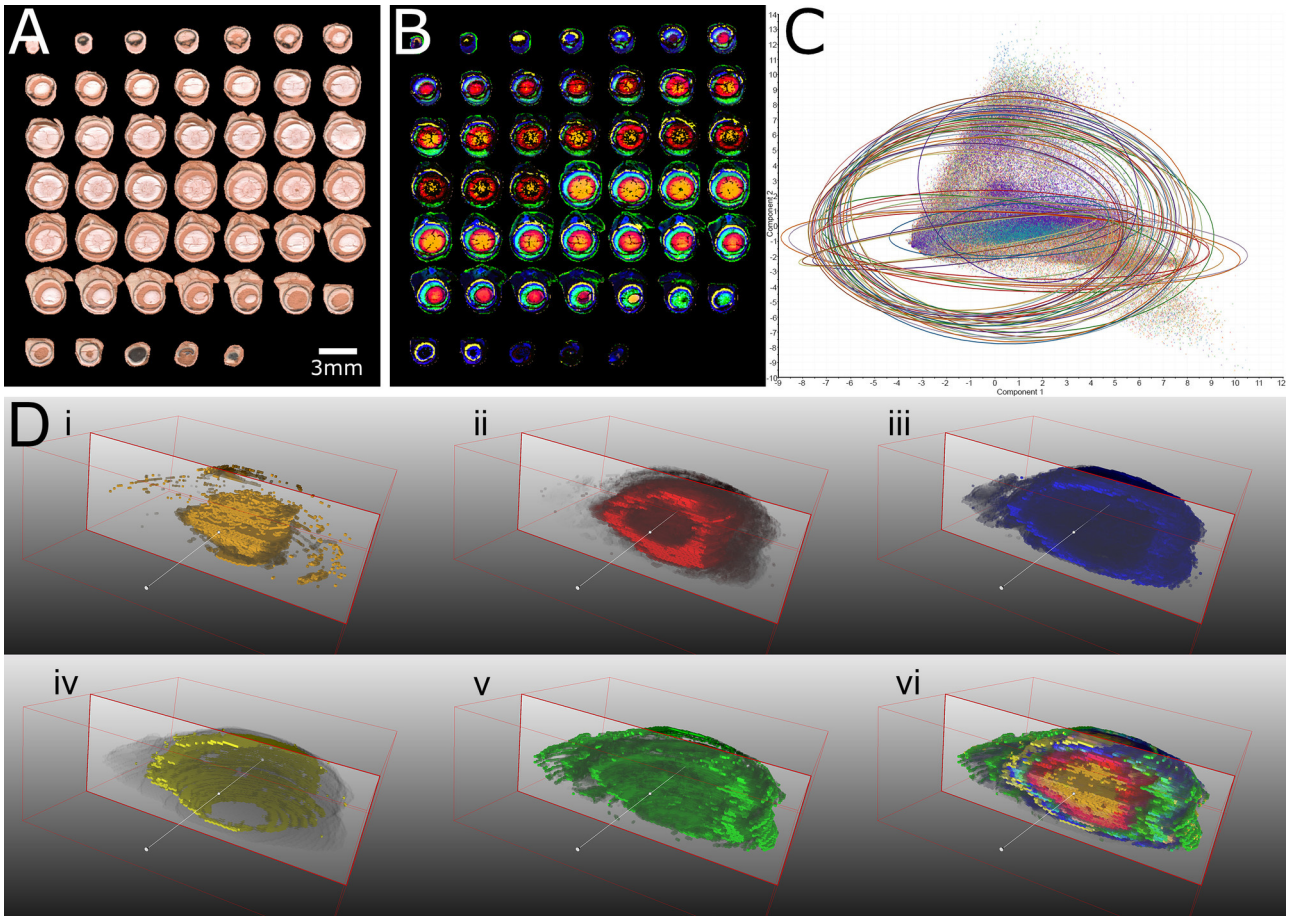

JMS_4460_Figure 6.jpg

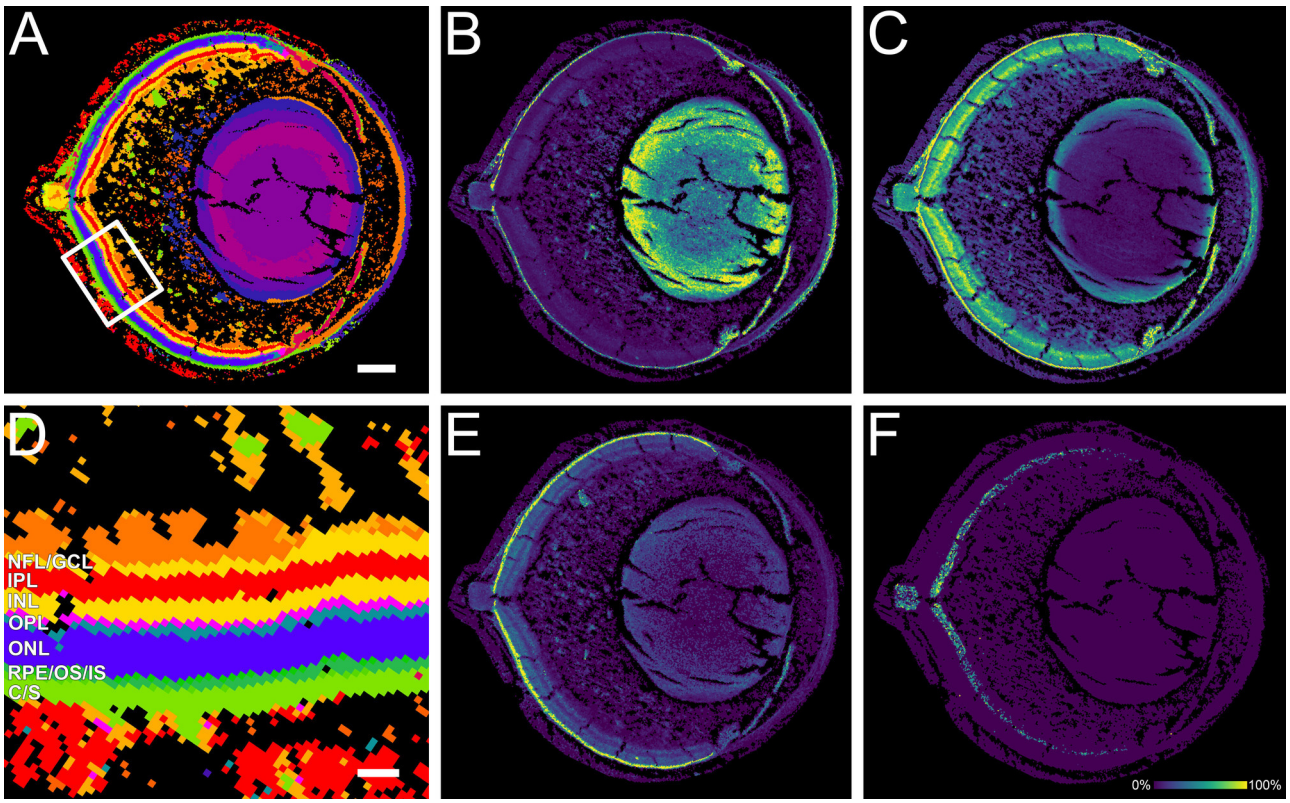

JMS_4460_Figure 7.jpg